
Article:
Chaplin, AK, Wilson, MT, Hough, MA et al. (5 more authors) (2016) Heterogeneity in the histidine-brace copper coordination sphere in auxiliary activity family 10 (AA10) lytic polysaccharide monooxygenases. Journal of Biological Chemistry, 291 (24). pp. 12838-12850. ISSN 0021-9258

https://doi.org/10.1074/jbc.M116.722447

Heterogeneity in the histidine-brace copper coordination sphere in AA10 lytic polysaccharide monooxygenases

Amanda K. Chaplin[1], Michael T. Wilson[1], Michael A. Hough[1], Dimitri A. Svistunenko[1], Glyn R. Hemsworth[2], Paul H. Walton[2], Erik Vijgenboom[3], Jonathan A.R. Worrall[1]

[1]School of Biological Sciences, University of Essex, Wivenhoe Park, Colchester, CO4 3SQ, U.K. [2]Department of Chemistry, University of York, Heslington, York, UK, YO10 5DD. [3]Molecular Biotechnology, Institute of Biology, Sylvius Laboratory, Leiden University, PO Box 9505, 2300RA Leiden, The Netherlands.

Running title: Binding of copper to LPMOs

To whom correspondence to be addressed: jworrall@essex.ac.uk; Tel: +44 (0)1206 872095

Key words: LPMO, EPR spectroscopy, kinetics, copper, *Streptomyces lividans*

ABSTRACT

Copper-dependent lytic polysaccharide monooxygenases (LPMOs) are enzymes that oxidatively deconstruct polysaccharides. The active site copper in LPMOs is coordinated by a histidine-brace. This utilises the amino group and side chain of the N-terminal His residue with the side chain of a second His residue to create a T-shaped arrangement of nitrogen ligands. We report a structural, kinetic and thermodynamic appraisal of copper binding to the histidine-brace in an auxiliary activity family 10 (AA10) LPMO from *Streptomyces lividans* (*Sli*LPMO10E). Unexpectedly we discover the existence of two apo-*Sli*LPMO10E species in solution that can each bind copper at a single site with distinct kinetic and thermodynamic (exothermic and endothermic) properties. The experimental EPR spectrum of copper-bound *Sli*LPMO10E requires the simulation of two different line shapes, implying two different copper bound species, indicative of three and two nitrogen ligands coordinating the copper. Amino group coordination was probed through the creation of an N-terminal extension variant (*Sli*LPMO10E-Ext). The kinetics and thermodynamics of copper binding to *Sli*LPMO10E-Ext are in accord with copper binding to one of the apo-forms in the wild-type protein, suggesting that amino group coordination is absent in the two nitrogen coordinate form of *Sli*LPMO10E. Copper binding to *Sli*LPMO10B was also investigated, and again revealed the presence of two apo-forms with kinetics and stoichiometry of copper binding identical to that of *Sli*LPMO10E. Our findings highlight that heterogeneity exists in the active site copper coordination sphere of LPMOs that may have implications for the mechanism of loading copper in the cell.

Lytic polysaccharide monooxygenases (LPMOs) are enzymes that utilize copper (Cu) as their functional active site metal and act to enhance the depolymerisation of recalcitrant polysaccharides in nature such as cellulose and chitin (1,2). Identification and characterisation of members of this cuproenzyme family from fungal and bacterial species has gathered pace in recent years due in part to their promising uses in biorefinery applications of biomass to derive second generation biofuels (2,3). LPMOs are classed into auxiliary activity (AA) families in the CAZy (Carbohydrate Active enZyme) database with four AA families, AA9, AA10, AA11 and AA13 so far identified (4). AA9 (formerly GH61) and AA10 (formerly CBM33) families have been the most extensively studied, with AA9 members having activity for cellulose, hemicellulose and cellodextrin substrates (5-8) and AA10 members having activity with either cellulose or chitin substrates (9,10). The AA11 and AA13 families are the most recently discovered and so far have been determined to have activity with chitin and starch substrates, respectively (11,12). All LPMOs

coordinate a single Cu ion by three nitrogen (N) ligands to from the active site. Two of these are provided from the amino group (Nt) and side-chain of the N-terminal His with the third from a second His side chain to give a T-shaped Cu coordination geometry referred to as the His-brace (6). To initiate enzymatic activity an electron source is utilised to reduce Cu(II) to Cu(I), with the latter required to activate dioxygen (13,14). Two principal mechanisms of glycosidic bond cleavage have been proposed (15,16) with the resulting C1 or C4 oxidation of a sugar ring (6,8,15,17-19) leading to chain breaks that are susceptible to hydrolases for further degradation.

Streptomycetes are the dominant bacterial genus responsible for aerobic biomass decomposition in soil environments and considered vital players in the decomposition of cellulose and other biomass polymers (20-22). Streptomycetes genomes encode a relatively high percentage of genes for putative celluloytic and chitinolytic enzymes. For example the secretome of *Streptomyces* sp. SirexAA-E (ActE) has been analysed through growth on a variety of carbon sources including cellulose and chitin (23). *Streptomyces coelicolor* and *Streptomyces griseus* have comparable putative genomic compositions of CAZy proteins to ActE, however these two streptomycetes are less capable of growing on cellulose (23). Thus not all streptomycetes, despite their abilities to grow on plant polysaccharides (21), are efficient cellulose decomposers.

In liquid-grown cultures, the growth of many streptomycetes is characterized by the formation of large, biofilm-like aggregates, called pellets (24,25). The competence of streptomycetes to directly secrete enzymes into the culture broth makes them attractive hosts for the heterologous production of commercially valuable enzymes (26,27). However, the pellets suffer from poor efficiency in oxygen and nutrient uptake and thus compromise the overall efficiency of the fermentation process. The synthesis of extracytoplasmic glycans is important for pellet formation (28-31). In *S. lividans* enzymes encoded by the *cslA-glxA* locus produce a β-(1,4)-glycan at the hyphal tip, of which the chemical composition is unknown (28-30). CslA belongs to the GlycosylTransferase Family 2, which includes cellulose and chitin synthases, amongst others (32). Deletion of *cslA* abolishes pellet formation in liquid-grown cultures and also blocks the formation of reproductive aerial hyphae on solid medium (28,29). GlxA is a newly characterized member of the AA5 family of mono-copper oxidase possessing a Tyr-Cys cross-linked redox cofactor (30). A *glxA* null-mutant blocks development and abolishes pellet formation coinciding with the loss of glycan deposition at hyphal tips – the same phenotype as observed with the *cslA* deletion (30,33). This is consistent with a model whereby CslA and GlxA cooperatively function in glycan deposition at the hyphal tip and are jointly responsible for the formation of reproductive aerial structures and, in liquid environments, for the formation of pellets (30).

Recent studies in *S. lividans* have identified an extracellular Cu-trafficking pathway involving two Cu chaperone proteins (Sco and ECuC) (34,35) and a DyP-type heme peroxidase (DtpA) (36) that are all required to facilitate GlxA maturation (*i.e.* Cu-loading and subsequent Tyr-Cys cross-link formation (30)). Based on these studies, a model has been developed that proposes the presence of a large protein complex at the hyphal tip for synthesis and deposition of the glycan required for morphogenesis (36). Downstream of *glxA* is the *cslZ* gene, encoding for an endoglucanase, whilst upstream of *cslA* is a gene (*SLI3182*), predicted to encode for an AA10 LPMO. The *S. lividans* genome has seven genes encoding putative AA10s (*Sli*LPMO10A-G) (37). RNA-seq data of *S. lividans* grown in a mannitol/glucose media reveals two *slilpmo10* transcripts to be constitutively expressed (*slilpmo10B* and *slilpmo10E*), whilst the remaining five may be under transcriptional control of a repressor or activator and depend upon induction by a polysaccharide substrate (Table 1).

In the present study we have set out to establish the biochemical and structural properties of *Sli*LPMO10E along with investigating the kinetic and thermodynamic properties of Cu(II) binding to the His-brace. Interestingly, our data is consistent with the His-brace of apo-*Sli*LPMO10E existing in two non-equilibrating forms that can coordinate Cu(II) by three or two N ligands. Mixed Cu(II) complexes of equal stoichiometry are also inferred from EPR spectral simulations, with the parameters derived indicating that AA10s

may not be as rhombic as originally thought but rather reflect a mixture of Cu(II) species.

EXPERIMENTAL PROCEDURES

Cloning of LPMOs and site-directed mutagenesis-A pET26b plasmid (Novagen) was modified by Quikchange mutagenesis to relocate the NcoI site 6 nt downstream. This modification enabled the over-expression of mature LPMOs correctly processed at the N-terminal His residue following cleavage of the *pelB*-leader sequence. *SLI3182* (nt 88 to 606) encoding for *Sli*LPMO10E and *SLI0614* (nt 127 to 687) encoding for *Sli*LPMO10B were amplified from *S. lividans* 1326 and cloned into the modified pET26b plasmid using the new NcoI and original HindIII restriction sites. Site-directed mutagenesis of His187 to an Ala in *Sli*LPMO10E was carried out by PCR using the wild type (WT) construct with forward and reverse primers containing the desired nucleotide change. The N-terminal *Sli*LPMO10E extension variant (*Sli*LPMO10E-Ext) whereby His30 is no longer the N-terminal residue was created by introducing a Gly residue prior to His30 and cloning into an unmodified pET26b plasmid to give a mature protein with an N-terminal sequence of Met-Gly-His. All constructs were DNA sequenced to corroborate the mutations and insertions.

Over-expression and purification of LPMOs-All proteins were over-expressed in *Escherichia coli* BL21 (RIL) cells starting from 37 ^{o}C overnight pre-cultures that were used to inoculate 500 ml LB cultures in 2 L flasks (37 °C, 180 rpm). At an OD_{600} of 0.4, the temperature was lowered to 16 °C and isopropyl β-D-1-thiogalactopyranoside (IPTG; Melford) was added to a final concentration of 1 mM on reaching an OD_{600} of 0.6. Cells were harvested after 16 h at 3,501 g for 20 min at 4 °C. Cell pellets were combined, weighed and resuspended in 1/30th of the total culture volume in ice-cold 50 mM Tris/HCl pH 8.0, 1 mM EDTA and 20 % w/v sucrose, and stirred at 4 °C for 1 h. For every gram of cell pellet 60 µl of 1 M $MgSO_4$ was added and stirring continued for a further 30 min at 4 °C. The smooth cell suspension was then centrifuged at 38,724 g for 20 min at 4 °C and the supernatant removed and stored at 4 °C. The pellet was then resuspended in ice-cold water (1/30th the volume of the culture), stirred at 4 °C for 1 h, followed by centrifugation at 38,724 g for 20 min with the supernatant collected and combined with that from the previous sucrose fractionation. The combined supernatants were then dialysed overnight against 5 mM Tris/HCl pH 7, 1 mM EDTA at 4 °C. For *Sli*LPMO10E (pI 8.42) and variants the dialysate was diluted with buffer A (5 mM Tris/HCl pH 7) and loaded to a 5 ml HiTrap SP-column (GE-Healthcare) equilibrated with buffer A and eluted with a linear salt gradient using buffer A containing 1 M NaCl. For *Sli*LPMO10B (pI 4.24) the dialysate was diluted with buffer B (10 mM Tris/HCl pH 5.5) and loaded to a pre-equilibrated DEAE column (GE-Healthcare) and eluted with a linear salt gradient using buffer B containing 500 mM NaCl. Fractions containing LPMO were pooled and concentrated at 4 °C using a 5 kDa cut-off centricon (Vivaspin). Concentrated protein was then loaded to a HiLoad 26/60 Superdex-75 column (GE Healthcare) equilibrated with buffer C (10 mM sodium acetate pH 5, 150 mM NaCl). Fractions eluting from the major peak were concentrated and used in subsequent experiments.

LPMO preparation-Protein concentrations were determined by UV-visible spectroscopy on a Varian Cary50 UV-visible spectrophotometer using an extinction coefficient (ε) at 280 nm of 36,690 M^{-1} cm^{-1} for *Sli*LPMO10E, H187A and *Sli*LPMO10E-Ext and 63,160 M^{-1} cm^{-1} for *Sli*LPMO10B (38). Prior to experiments requiring the addition of Cu(II) salts proteins were incubated for prolonged periods with excess EDTA followed by gel-filtration. For Cu(II) titrations and preparation of Cu(II)-loaded enzyme a stock solution of 100 mM Cu(II)SO_4 (Sigma) was prepared and diluted as required. Cu(II)-loaded enzymes were prepared by stoichiometric addition of Cu(II)SO_4 followed by desalting to ensure no unbound metal remained.

Substrate binding assay-*Sli*LPMO10E (~ 20 µM in 50 µl of 50 mM Bis-Tris/HCl pH 6.2) was incubated with ~ 5-10 mg of excess substrate; cellulose (Whatman #1, 50 µm), or squid pen β-chitin at room temperature for 3-4 h with occasional agitation. The supernatant was then removed by centrifugation and kept as the unbound fraction. Substrate was then washed three

times to remove any unspecific enzyme. Bound enzyme was removed by adding 50 µl of SDS-PAGE loading buffer containing DTT and heating at 95 °C for 10 min. Samples were then analysed for bound and unbound enzyme content using a 15 % SDS-PAGE gel (BioRad).

Mass spectrometry-Oxidative activity was assayed by mass spectrometry (MS) using a range of substrates (squid pen β-chitin, Avicel (cellulose), Konjac glucomannan, Guar gum, Ivory nut mannan and Locust bean gum). Reaction mixtures (1 ml total volume) contained 0.2 % w/v solid substrate in 10 mM ammonium acetate, pH 5., 1 mM ascorbic acid and 10 µM Cu-loaded LPMO. Control samples were also prepared in the absence of ascorbic acid and protein. Reactions were incubated at 30 °C rotating for 5-12 h before the remaining solid substrate was removed by centrifugation at 16,000 g, 4 °C for 5 min and the supernatant used for analysis. 1 µl of sample was mixed with an equal volume of 10 mg/ml 2,5-dihydroxybenzoic acid in 50 % acetonitrile, 0.1 % trifluoroacetic acid on a SCOUT-MTP 384 target plate (Bruker). The spotted samples were then dried in a vacuum desiccator before being analyzed on an Ultraflex III matrix-assisted laser desorption ionization–time of flight/time of flight (MALDI-TOF/TOF) instrument (Bruker), as described previously (9).

Electron Paramagnetic Resonance (EPR) spectroscopy and spectral simulations-Samples (80 µM) for EPR analysis were prepared in duplicate in 5 mM Tris/HCl pH 7, 150 mM NaCl with additions of 0.9 equivalent of Cu(II)SO_4. Wilmad SQ EPR tubes (Wilmad Glass, Buena, NJ) were filled with 250 µl LPMO solutions and frozen in methanol kept on dry ice, then transferred to liquid nitrogen. All EPR spectra were measured at 10 K on a Bruker EMX EPR spectrometer (X band). A spherical high-quality Bruker resonator ER 4122 SP 9703 and an Oxford Instruments liquid helium system were used to measure the low-temperature EPR spectra. Blank spectra of frozen water samples were subtracted from the EPR spectra of the protein samples to eliminate the baseline caused by the resonator's walls, quartz insert or quartz EPR tube. The baseline was corrected by subtracting a polynomial line drawn through a set of points randomly chosen on the baseline using WinEPR (v2.22, Bruker Analytik, GmbH). Spectral simulations were performed in SimFonia v. 1.26 (Bruker Analytik, GmbH). The g_z value and its hyperfine splitting constant A_z^{Cu} were determined directly from the spectra. Rather than varying g_x and g_y independently, two other values, g_{av} and Δg, were varied, where $g_{av} = (g_x + g_y)/2$ and $\Delta g = g_y - g_{av} = g_{av} - g_x$. To maintain consistency in the simulation procedure while varying the minimal number of parameters, a number of constraints were imposed on the choice of the other simulation parameters thus minimising the number of varied parameters. Thus, the tensor for the hyperfine interaction of the spin density with Cu nucleus A^{Cu} (I_{Cu} = 3/2) was assumed axial, with the $A_x^{Cu} = A_y^{Cu} = 0.1\ A_z^{Cu}$ (small variations around empirically picked factor of 0.1 were found to produce minimal effect on the simulated spectra). Furthermore, all A^{Cu} tensors were assumed collinear with the g-tensor (all Euler angles were assumed zero). Cu(II) coordinating nitrogen atoms (I_N = 1) were assumed to produce isotropic hyperfine interactions ($A_x^N = A_y^N = A_z^N$ = 14 G). In accordance with earlier reported relationship between principal g-factor components and individual line width values along those directions (39), the x-, y- and z- components of the spectra line width ΔH were assumed to have a close to linear dependence on the g-values, the higher the g_i, the higher the ΔH_i value. This dependence was maintained for all simulations.

Fluorescence spectroscopy-Fluorescence spectroscopy was carried out at 20 °C on a LS 50B fluorimeter (Perkin Elmer) with emission spectra collected between 300 and 400 nm following excitation at 295 nm. The excitation emission slit widths were both set at 5 nm. LPMO proteins (2 µM) were prepared in 10 mM sodium acetate pH 5, 150 mM NaCl and titrated with microliter aliquots of a Cu(II)SO_4 solution.

Stopped-flow kinetics-Kinetic experiments to measure fluorescence emission changes on Cu(II) binding were carried out on a SX20 stopped-flow spectrophotometer (Applied Photophysics) thermostatted at 25 °C. Trp residues were excited at 295 nm and emitted fluorescence sampled at right angles to the exciting beam after passage

through a cut-off filter permitting light with wavelengths above 350 nm to pass, thus removing any scattered exciting light. All LPMO samples (2.5 or 5 μM after mixing) were prepared in 10 mM sodium acetate, pH 5, 150 mM NaCl and were rapidly mixed with a range of $Cu(II)SO_4$ concentrations (25-500 μM after mixing). Following excitation at 295 nm time courses were taken collecting the total fluorescence emission. Stoichiometry of Cu(II) binding to the LPMOs was monitored by fluorescence amplitude changes. All kinetic data were analysed using the ProKinetist software (Applied Photophysics).

Isothermal titration calorimetry (ITC)-Calorimetric titration experiments were carried out at 25 ± 0.1 ^{o}C on a MicroCal VP-ITC calorimeter in (10 mM sodium acetate pH 5, 150 mM NaCl). Before each run, samples were degassed for 15 min at 23 ± 0.1 ^{o}C using the ThermoVac accessory. A solution of $Cu(II)SO_4$ (1 mM) was loaded into the injection syringe and titrated into 100 μM of WT or variant *Sli*LPMO10E in the sample cell with stirring at 307 rpm for the duration of the experiment. A reference power of 5 μcal/s was used with either an initial 3 or 5 μl injection of $Cu(II)SO_4$ followed by either 5 or 10 μl injection for all subsequent titration points. A 60 s initial equilibrium delay with 270 s pauses between subsequent injections were applied throughout. Raw data were analysed using Origin 7.0 software. The integrated data were corrected for the heat of dilution of buffer into buffer and $Cu(II)SO_4$ into buffer and the binding isotherms were fitted using binding models provided in the software package.

Crystallisation and structure determination-An ARI-Gryphon 96-well crystallisation robot was used to screen crystallisation conditions for *Sli*LPMO10E. A crystal hit was found in 0.1 M sodium acetate pH 4.6, 25 % PEG 4,000 (PEG suite, Qiagen). Scaling-up and optimisation of *Sli*LPMO10E crystals from the initial hit were carried out in 24-well VDX plates (Molecular Dimensions) using the hanging drop vapor diffusion method at 18 ^{o}C. Equal volumes of protein (15 mg ml^{-1}) and reservoir solution were mixed and crystals suitable for diffraction studies grew within 2-3 weeks. A single crystal grown from 0.05 M sodium acetate pH 4.6, 25 % PEG 4,000 was transferred to a cryoprotectant solution containing, the respective reservoir solution and 20 % glycerol prior to flash-cooling by plunging into liquid nitrogen. Crystallographic data were measured at beamline I03, Diamond Light Source, using an X-ray wavelength of 1.00 Å and a Pilatus 6 M-F detector (Dectris). Data were processed automatically using XDS (40) in XIA2 (41) and scaled and merged using Pointless/Scala (42) in the CCP4i suite. The structure was solved using automated molecular replacement in BALBES with an initial model built in Arp-Warp (43,44). The structure was refined using Refmac5 (45), with model building between refinement cycles in Coot (46). Riding hydrogen atoms were added when refinement of the protein atoms had converged. Structures were validated using the Molprobity server (47), the JCSG Quality Control Server and tools within Coot (46). Coordinates and structure factors were deposited in the RCSB Protein Data Bank. A summary of data, refinement statistics and the quality indicators for the structure are given in Table 2. Additional datasets were collected at wavelengths of 1.20 Å and 1.33 Å to generate anomalous maps for validation of modelled Cu atoms in the structure (Table 2).

RESULTS

Trp fluorescence of apo-SliLPMO10E is quenched upon binding Cu(II)-Size-exclusion chromatography revealed *Sli*LPMO10E to be a monomeric species, which migrated as a single band on a SDS-PAGE gel to a mass of ~ 18 kDa (predicted mass 18,422 Da for residues 30-201). Samples of as-purified *Sli*LPMO10E were subjected to ICP-MS analysis and a Cu content of < 3 % (0.03 μg atoms/L) was consistently determined, indicating a predominately apo-form. Titrating Cu(II) into apo-*Sli*LPMO10E resulted in the quenching of the Trp fluorescence at λ 340 nm (Figure 1), with a break point reached at ~ 0.8 to 0.9 equivalents of Cu, indicating a binding stoichiometry close to 1:1 (Figure 1).

X-band EPR spectroscopy infers the existence of two Cu(II) complexes-Apo-*Sli*LPMO10E gave a very weak EPR signal consistent with the presence in the sample of a small amount of Cu(II), in agreement with ICP-MS analysis (Figure 2A). On preparation of holo-*Sli*LPMO10E, a much stronger

EPR signal clearly originating from Cu(II) centres is obtained (Figure 2B). Attempts to simulate this experimental spectrum as a single Cu(II) species proved unsuccessful. However, a simulation was possible if a linear combination of two different line-shapes was assumed (Figure 2C) with the simulation parameters reported in Table 3. Thus the experimental EPR spectrum recorded at 10 K for *Sli*LPMO10E is best approximated by a superposition of two different EPR lines, further referred to as Sim1 and Sim2, from two different Cu(II) complexes. Sim1 was simulated for three N atoms coordinating Cu and Sim2 for two N atoms. One noticeable difference between the line shapes of Sim1 and Sim2 is the presence of a strong 'overshoot' line in Sim2. This is a consequence of a combination of two factors: a smaller g-factor anisotropy (resulting in a smaller g_z value) and a larger Az^{Cu} value in Sim2, than in Sim1 (Table 3). The second integrals of Sim1 and Sim2 are similar within 2 % accuracy indicating the two Cu(II) complexes are likely to be present in roughly equal concentrations.

SliLPMO10E has enzymatic activity with β-chitin-Initial substrate binding experiments using cellulose and β-chitin were monitored by SDS-PAGE. *Sli*LPMO10E displayed a clear preference for β-chitin based on the proportion of unbound relative to bound fraction observed on the gel (inset Figure 3). Substrate specificity and activity was further probed by incubation with diverse glycan substrates (see Experimental Procedures) in the presence of ascorbate as the reducing agent. MALDI-TOF MS analysis of the reaction products revealed LPMO activity only for β-chitin (Figure 3). The observed activity was mainly consistent with previous studies on chitin-active AA10s (9), producing predominantly reducing-end aldonic acid oligosaccharide products (C1 oxidation) with even numbered degrees of polymerization. However, not consistent was the observation of -2 Da species implicated as possible reducing end lactones prior to ring opening, or non-reducing end ketoaldoses resulting from C4 oxidation (Figure 3). Distinguishing these species by MS is challenging and so from this present data it is unclear whether *Sli*LPMO10E is capable of oxidizing at the C4 as well as the C1 position.

X-ray crystal structure of SliLPMO10E reveals two Cu binding sites-The X-ray structure of holo-*Sli*LPMO10E was determined to a resolution of 1.38 Å and contains one protein molecule in the crystallographic asymmetric unit. Continuous and well-defined electron density was found for residues 30 to 201. The overall structure comprises seven anti-parallel β-strands arranged in two β-sheets (Figure 4A); one containing three antiparallel strands (S1, S3, S6) and the other, four antiparallel strands (S4, S5, S7, S8). This distorted β-sandwich fold is consistent with that of other AA10 structures (48-52). Between strands S1 and S3 is the Loop 2 region, which shows the most variability in size between LPMO families. In *Sli*LPMO10E this region consists of two α-helices (H1 and H2) and a small β-strand (S2). Two disulfide bonds are also present, Cys43/Cys51 and Cys78/Cys196, with the latter connecting Loop 2 to the C-terminal β-strand (S8) (Figure 4A). Disulfide bonds have been identified in other LPMOs and most likely confer structural stability.

A well-defined 16-σ peak is observed in the σA-weighted F_o-F_c difference map into which a Cu ion was modelled with coordination by three equatorial nitrogen ligands; the Nt of His30 and the Nδ1 and Nε2 atoms of His30 and His120, respectively (Figure 4B). This results in the T-shaped His-brace coordination geometry, with bond lengths and angles reported in Table 4. A number of residues commonly found in chitin-active AA10s are noted and include Ala118, suggested to influence the solvent facing Cu site and Phe193 (52) (Figure 4B). The latter lies with its Cζ atom only 3.6 Å from the active site Cu, a feature consistently found in AA10s but replaced by Tyr in the cellulose active *S. coelicolor* *Sc*LPMO10B (a homologue to *Sli*LPMO10B) (52). The side chain orientations of Glu62 and Val186 in the vicinity of the Cu site make a cavity, which is a feature found in other chitin-active AA10s and has been suggested to accommodate oxygen or the acetyl group of an N-acetyl glucosamine moiety (52).

The putative substrate-binding surface of *Sli*LPMO10E is flat with two small stretches of opposite surface charge, running either side of the positively charged Cu ion (Figure 4C). A prominent surface aromatic residue, Trp56 is

located in the Loop 2 region, and is considered important in AA10s for substrate specificity.

A second well-defined σ-peak in the σA-weighted F_o-F_c difference map consistent with the presence of a metal ion is also observed. Modelling a Cu ion into this peak results in coordination with His187 and Asp188 from the monomer in the asymmetric unit and the same residues from a symmetry related molecule, thus creating a metal mediated dimer (Figure 5A). Crystallisation conditions contained no metal-salts and the excess of Cu(II) used to form the holo-*Sli*LPMO10E was removed prior to crystallisation. Although every care was taken to ensure no serendipitous binding of rogue metals, there is the possibility that a divalent metal such as Zn(II) could out compete Cu(II) for this site. Therefore, to confirm the identity of the metals in both sites (Cu or Zn), anomalous difference maps were generated by measuring a single crystal at two different X-ray wavelengths (1.2 Å and 1.33 Å). At 1.2 Å the energy is above that of both Cu and Zn K-edges, whereas at 1.33 Å only the Cu K-edge contributes to the anomalous scattering. Anomalous maps generated at these different wavelengths for both the active and dimer sites are consistent with the presence of a Cu ion in both sites (Figure 5B). The Cu coordination geometry in the symmetry generated dimer is a distorted square planar, with the Nε2 atoms of the His residues coordinating in a linear fashion and the Oδ2 atoms of the aspartates bent (Table 4). The existence of such a metal mediated dimer is not readily supported from solution measurements (Figure 1).

Kinetics of Cu(II) binding to apo-SliLPMO10E reveals two binding forms- Apo-*Sli*LPMO10E was mixed with Cu(II) solutions of known concentrations and the quenching of Trp fluorescence monitored as a function of time in a stopped-flow spectrophotometer. Upon mixing, two phases of fluorescence quenching were observed, the rates of which were [Cu(II)] dependent (Figure 6A and inset). Pseudo first-order rate constants (k_{obs}) were linearly dependent on the [Cu(II)], with the slopes yielding second-order rate constants, k_1 and k_2 (Figure 6A inset and Table 5). The linear plots run through/close to the origin, indicating that the Cu(II) affinity of the binding sites are high (*i.e.* the dissociation rate constants for Cu(II) are small compared to the association rates) and the relative amplitudes of the two phases are independent of the [Cu(II)]. Binding stoichiometries were measured by first loading apo-*Sli*LPMO10E with *sub* to *super* stoichiometric amounts of Cu(II) followed by mixing with excess Cu(II). Upon mixing, the two phases were retained, but as expected the total amplitude of the fluorescence quench decreased as the concentration of the Cu(II) preloaded into *Sli*LPMO10E increased (*i.e.* Cu(II) can now only bind to the empty sites). The relative amplitudes of the two phases changed as a result of pre-mixing with Cu(II), the faster phase being abolished at lower preloaded Cu(II) additions and the slow phase at higher preloaded [Cu(II)]. This enables the stoichiometry of each phase to be determined as illustrated in Figure 6B. The faster phase titrated with a stoichiometry of ~ 0.5, and the slower phase, which titrates once the site responsible for the faster binding is filled, also with a stoichiometry of ~ 0.5. Thus, the overall stoichiometry is 1:1, consistent with the interpretation of the static fluorescence titration (Figure 1). Furthermore, the proportions of the two kinetic phases are unaffected at low [NaCl]. Therefore the observed [Cu(II)] dependence is not an ionic strength effect and the data are consistent with Cu(II) binding to two forms of a single site.

The two [Cu(II)] dependent phases observed in the kinetic measurements prompted us to consider whether the slow phase of Cu(II) binding was due to the presence of a second Cu binding site. Kinetic experiments, with the H187A variant gave essentially identical results to that of the WT *Sli*LPMO10E *i.e.* two clear phases both [Cu(II)] dependent with k_1 and k_2 values reported in Table 5. Thus, the contribution of this dimer site observed in the crystal structure to the quenching of fluorescence in the WT protein may be discounted.

ITC identifies two thermodynamically distinct Cu(II) binding sites-A typical ITC profile obtained by titrating Cu(II) into apo-*Sli*LPMO10E is shown in Figure 7, where two binding phases are detected. The first of these is an exothermic process with the second endothermic in nature. A two-site model was used to fit the data with the parameters obtained reported in Table 5. Notably, the stoichiometry (N) for each binding phase is ~

0.5 giving a total stoichiometry of 1 and thus in keeping with the kinetic data. The first binding phase has a nM K_d for Cu(II) and exhibits a favourable enthalpic binding (ΔH_b) contribution, with a small but favourable entropic ($-T\Delta S$) contribution leading to a favourable free energy of binding (ΔG_b) (Table 5). The second phase displays a weaker affinity for Cu(II) with a μM K_d (Table 5). Moreover, this binding event is characterised by a positive ΔH_b (unfavourable) that is compensated for by an increased $-T\Delta S$, thus maintaining a favourable ΔG_b (Table 5). The H187A mutant gave the same ITC profile with the parameters obtained from fitting to a two-site model comparable to WT *Sli*LPMO10E (Table 5), reconfirming that the second metal site observed in the crystal is not that detected by either kinetics or ITC.

The kinetics of Cu(II) binding to SliLPMO10B are identical to those of SliLPMO10E-To investigate whether the complex kinetics of Cu(II) binding is unique to *Sli*LPMO10E or may be typical for AA10s a second AA10 was tested. *Sli*LPMO10B is a homolog of *Sc*LPMO10B from *S. coelicolor* whose structure has been reported and is cellulose active (52). Size-exclusion chromatography of purified *Sli*LPMO10B revealed a monomer species which migrated as a single band on a SDS-PAGE gel to a mass of ~ 20 kDa (predicted mass 20,723.4 Da for residues 43-229). Trp fluorescence at $\lambda \geq 350$ nm was quenched upon addition of Cu(II) aliquots, until a break point at ~ 0.8 to 0.9 equivalents was reached, indicating a binding stoichiometry close to 1:1. On rapid mixing in the stopped-flow with excess Cu(II) the fluorescence was quenched as seen for *Sli*LPMO10E with time courses again found to comprise two phases, the rate constants of which were linearly dependent on [Cu(II)] (Table 5).

Cu(II) binding to the SliLPMO10E-Ext variant reveals a single Cu(II) form-The mature *Sli*LPMO10E-Ext variant has a Met-Gly-His N-terminal sequence and was produced with the aim to abolish/perturb the Nt coordination of the His-brace. *Sli*LPMO10E-Ext remains capable of binding Cu(II) as determined from the quenching of the Trp fluorescence. However, in contrast to *Sli*LPMO10E where the tight binding of Cu(II) precluded the determination of a K_d (Figure 1), *Sli*LPMO10E-Ext possesses a weaker affinity for Cu(II) enabling a K_d to be determined (Table 5). Stopped-flow fluorescence measurements yielded time courses now comprising of three phases after mixing with excess Cu(II). The fastest phase was linearly dependent on [Cu(II)] (Figure 8A) with a second order rate constant (k_1) reported in Table 5. Although binding to this site is rapid it is with low affinity as seen by the intercept on the k_{obs1} axis, which is interpreted as the dissociation rate constant (k_{off}) of Cu(II) from this site ($k_{off} = 230\ s^{-1}$) (Figure 8A) enabling a K_d of 1.2×10^{-4} M to be determined. The two slower phases display little [Cu(II)] dependence and are assigned to first order reorganisation steps (k_2 and k_3 Table 5) in the Cu(II)-bound *Sli*LPMO10E-Ext that each lead to enhanced quenching of the Trp fluorescence. Titration experiments performed by mixing Cu(II) solutions with *Sli*LPMO10E-Ext preloaded with *sub* to *super* stoichiometric [Cu(II)] were also carried out. Unlike for *Sli*LPMO10E the three distinct phases all titrate together indicating binding to a single site that undergoes rearrangement. A striking result is that the K_d determined following preloading with Cu(II) (Figure 8B and Table 5), is two orders of magnitude lower (tighter) than the initial (fast) binding site (K_d 1.2×10^{-4} M) and in line with the K_d determined from static fluorescence titration experiments (Table 5). Together these indicate that following initial Cu(II) binding, subsequent rearrangements detected in the slower kinetic phases lock Cu(II) into the site. This is supported by the observed decrease in the amplitude of the slower phase as the [Cu(II)] with which it is mixed increases. This is expected when the [Cu(II)] span the value of the K_d for the initial binding site. Thus, at 100 μM Cu(II) the amplitude of the fast phase reflects half occupancy of this site, full binding then occurs at the rate of the slower phase. At 250 μM Cu(II), approximately 70 % of the initial site is rapidly filled and reflected in the amplitude of the initial binding process and the remaining sites are filled at the rate of the reorganisation.

The ITC profile in Figure 8C shows an endothermic binding event, fitted to a single-site binding model to give the parameters reported in Table 5 for Cu(II) binding to *Sli*LPMO10E-Ext. A stoichiometry of ~1 Cu(II) is determined with a K_d

in the μM range correlating well to that determined from the static fluorescence titration and stopped-flow kinetics (Table 5). The unfavourable ΔH_b is compensated for by a large favourable -TΔS contribution, maintaining a favourable ΔG_b (Table 5). Thus the thermodynamic profile for the *Sli*LPMO10E-Ext variant has a strong resemblance to the second endothermic binding event observed with the WT *Sli*LPMO10E.

DISCUSSION

Two cellulose degrading AA10s from *S. coelicolor* (*Sc*LPMO10B and *Sc*LPMO10C) and a chitin degrading AA10 from *S. gresius* (*Sg*LPMO10F), have so far been characterised from streptomycetes (52-54). *Sc*LPMO10C and *Sg*LPMO10F have been shown to oxidise strictly at the C1 carbon of the sugar (52,54), whereas *Sc*LPMO10B can oxidise at the C1 and C4 positions (52). *Sli*LPMO10E is active only on chitin, with the predominant oxidation product revealed from MS indicative of C1 cleavage (Figure 3). As described for other AA10s, a Phe and a conserved Ala residue are located in the vicinity of the Cu site, with their hydrophobic side chains orientated so as to impede access/binding of exogenous ligands to the axial positions of the Cu ion (Figure 4B) (51,55). This has led to the suggestion that dioxygen activation is most likely at the fourth equatorial position in AA10s resulting in strict C1 substrate oxidation. Conversely, access to the solvent-facing axial position has been suggested to be responsible for C1/C4 oxidation in AA9s lacking an Ala and in *Sc*LPMO10B where the Ala is present but the side chain is positioned so as not to obstruct ligand access (16,52). In *Sli*LPMO10E the Ala118 side chain superimposes with other strict C1 oxidising AA10s. This structural feature is consistent therefore with the MS interpretation of C1 oxidised products of the chitin substrate and furthermore predicts that the -2Da species identified in the MS likely arises not from C4 oxidation products but reducing end lactones.

Whilst a major focus of LPMOs has been on their roles and activities with biomass derived polysaccharides substrates, the constitutive expression and proximity of *slilpmo10E* to the *cslA-glxA* operon could imply a role in assisting with the attachment or further processing/modification of the *cslA-glxA* glycan produced during the development cycle. The chemical composition of this glycan essential for morphological development in *S. lividans* has not yet been characterized. Typically, genes involved in bacterial cellulose synthesis are organized in an operon, containing the *bcsABCD* genes (56). However, *Streptomyces* lacks a c-di-GMP binding protein (BcsB), conserved in cellulose-producing organisms and essential for the synthesis of cellulose (57). In light of this and the activity of *Sli*LPMO10E only for chitin hints at the possibility that the glycan produced by CslA has N-acetyl glucosamine functionalities.

The X-ray crystal structure of *Sli*LPMO10E reveals the active site Cu to have the characteristic His-brace coordination associated with all other LPMOs (Figure 4). A second coordinating Cu ion was also identified in the X-ray structure, with subsequent solution studies providing no evidence to indicate that this second Cu site is occupied or that the metal mediated dimer that can be generated in the crystal is formed. Despite this, the orientation of the two monomers is noteworthy (Figure 5), as dimerization does not occlude the substrate interaction surface.

Spectral simulation (Sim1 and Sim2) of the EPR spectrum of *Sli*LPMO10E indicates the presence of two Cu(II) species. The g_z and A_z^{Cu} values for these are 2.26/2.23 and 135/190 G respectively, with the 2.26 and 135 G pair representing the 'typical' distorted AA10 coordination where the three N atoms of the His brace are all coordinating to the Cu(II). The g_z and A_z^{Cu} values determined directly from the spectral parallel region are the most reliable parameters for comparison with EPR data obtained from other LPMOs. In contrast the perpendicular g values (g_x and g_y) are estimated through simulation. From the present study it is clear that the simulation of spectra for a mixed species gives a significantly lower degree of rhombicity (difference between g_x and g_y) compared to other AA10s (51,53). Thus previous AA10 values, whilst recognizant of the difficulty of simulating g_x and g_y values, may reflect a mixture of species rather than true rhombicity (51). For chitin active AA10s A_z values of between 109 and 118 G have been reported (53), placing them between the normal

Peisach-Blumberg classification of type 1 and type 2 Cu centres (58). In contrast cellulose active AA10s and AA9s have higher A_z values of *c.a.* 147 G and are firmly within the type 2 classification (53). Thus *Sli*LPMO10E lies in between cellulose active AA9s/AA10s and chitin active AA10s, suggesting a more axial geometry compared to other chitin active AA10s. The second species has a lower g_z value of 2.23 and is in a clearly axial geometry (A_z = 190 G). This could arise from a Cl ion binding to the Cu(II), as a consequence of 150 mM NaCl being present in the buffer, in accord with the g_z value of 2.23 recently determined for an AA9 LPMO where Cl acts as the exogenous ligand on Cu(II) (59). The axial geometry may arise from two N atoms coordinating to the Cu(II), with the decomplexation of one of the His residues or the Nt a possibility, with the coordinated mono-atomic Cl ion able to move around until it overlaps well with the $d(x_2\text{-}y_2)$ orbital giving rise to the lower g_z of 2.23 owing to enhanced covalency of the SOMO across the Cl ligand (59).

In vitro Cu(II) binding studies to *Sli*LPMO10E and *Sli*LPMO10B are most consistent with the mechanism depicted in Figure 9. Our data suggest that the as isolated apo-form of these AA10s exist as two non-equilibrating species (I and I* Figure 9). Cu(II) first binds to species I in an exothermic reaction with a nM K_d, which we attribute to Cu(II) coordinating all three N ligands of the His-brace. Once the Cu(II) binding site in species I is filled, the second apo-species (I*) binds Cu(II) in an endothermic manner with a μM K_d, and is attributed to Cu(II) coordinating two N ligands of the His brace, with H_2O (low salt conditions) or Cl ions (high salt conditions) completing the equatorial coordination sphere (X in Figure 9). Thus, under the conditions investigated (low and high salt), Cu(II) binds to a single site in two binding forms, each with distinct kinetic and thermodynamic parameters (Figure 9, Table 5). Comparison of the kinetic and thermodynamic data for the *Sli*LPMO10E-Ext variant with that of the WT gives a strong indication that the two coordinate N species arises from the absence of Nt coordination (Figure 9 and Table 5). This interpretation arises from the unfavourable ΔH_b and K_d that mirror the second binding form of the WT protein (overall K_d 10^{-6} M) and the presence of a single Cu(II) dependent binding step (Table 5). The proposition that the kinetics and EPR results arise from two forms of a single site must be set against the structural data that shows a single unique Cu binding configuration. One way to account for this apparent discrepancy is by proposing that one of the forms discerned in the kinetic experiments resides at lower energy than the other form. Once Cu(II) is bound the whole of the protein slowly converts to the lower energy form with the Nt moving inwards and completing the three coordinate His-brace geometry as seen in the X-ray crystal structure (dashed arrow Figure 9). This final conversion would be difficult to detect in fluorescence experiments, as it would occur in the Cu(II) bound form in which fluorescence is largely quenched.

The fact that we have observed heterogeneity in the His-brace coordination geometry in all batches of *Sli*LPMO10E and *Sli*LPMO10B prepared, lends credence to the view that coordination flexibility is inherent in the His-brace motif. The question therefore arises as to what biological function this may be assigned to. It is possible that the two forms have different enzymic functions, or the flexibility of the Cu site is important for loading Cu from an *in vivo* donor (i.e. chaperone or low molecular weight ligand). In this respect any putative donor will have a very high affinity for Cu with the metal only being transferred through docking and orientating the donor and acceptor ligands to enable facile metal transfer through a ligand exchange mechanism (60). Here we are loading Cu in a way that would never happen *in vivo*, namely Cu is added in large excess in a non-coordinating form. Therefore what we may be observing is a heterogeneity of the metal binding site that in some way reflects different states of the protein, which maybe populated transiently in the true biological transfer. Finally, it is worth considering that these AA10s are Sec substrates and fold following translocation across the membrane. As the protein passes into the extracellular space Cu may become quickly bound (via a chaperone or low molecular weight ligand) prior to cleavage of the signal sequence that then enables for the final N coordination by the Nt. This is reminiscent of Cu binding to the Ext-mutant that incorporates the metal into a *single* site, which once undergone rearrangement binds Cu tightly (Figure 9). If this

happens with the signal sequence in place then cleavage and coordination of the final N ligand occurs when the site is already full. The as purified WT LPMO proteins lack the signal sequence and in its absence result in two species. These can adopt two folded forms of the His-brace in the apo-state (Nt "out" or "in") that upon *in vitro* Cu loading result in the heterogeneity observed, whereas the Ext-mutant may replicate the true mechanism of Cu binding *in vivo*.

ACKNOWLEDGEMENTS
The award of a University of Essex Silberrad PhD scholarship to AKC is gratefully acknowledged. Professor R. Hider for access to ICP-MS measurements at the Institute of Pharmaceutical Science, King's College London. Dr Dennis Claessen for critical reading of the manuscript. Diamond Light Source for access to beamline I03 (East of England Macromolecular Crystallography BAG, MX7461) and use of the JCSG Quality Control Server is acknowledged.

CONFLICTS OF INTERESTS
Authors declare no conflict of interest

AUTHOR CONTRIBUTIONS
A.K.C. conducted all experiments, prepared all samples and analysed all data. M.T.W. assisted with stopped-flow experiments and analysed the data. M.A.H. supervised the crystallography and structure determination. D.A.S. carried out EPR experiments and spectral simulations. P.H.W and G.R.H contributed reagents, mass spectrometry and EPR discussion. E.V. carried out RNA-seq analysis. J.A.R.W designed the study and wrote the manuscript with contributions from all co-authors.

REFERENCES

1. Beeson, W. T., Vu, V. V., Span, E. A., Phillips, C. M., and Marletta, M. A. (2015) Cellulose degradation by polysaccharide monooxygenases. *Annu. Rev. Biochem.* **84**, 923-946
2. Hemsworth, G. R., Johnston, E. M., Davies, G. J., and Walton, P. H. (2015) Lytic Polysaccharide Monooxygenases in Biomass Conversion. *Trends Biotechnol.* **33**, 747-761
3. Muller, G., Varnai, A., Johansen, K. S., Eijsink, V. G., and Horn, S. J. (2015) Harnessing the potential of LPMO-containing cellulase cocktails poses new demands on processing conditions. *Biotechnol. biofuels* **8**, 187
4. Lombard, V., Golaconda Ramulu, H., Drula, E., Coutinho, P. M., and Henrissat, B. (2014) The carbohydrate-active enzymes database (CAZy) in 2013. *Nucleic Acids Res.* **42**, D490-495
5. Harris, P. V., Welner, D., McFarland, K. C., Re, E., Navarro Poulsen, J. C., Brown, K., Salbo, R., Ding, H., Vlasenko, E., Merino, S., Xu, F., Cherry, J., Larsen, S., and Lo Leggio, L. (2010) Stimulation of lignocellulosic biomass hydrolysis by proteins of glycoside hydrolase family 61: structure and function of a large, enigmatic family. *Biochemistry* **49**, 3305-3316
6. Quinlan, R. J., Sweeney, M. D., Lo Leggio, L., Otten, H., Poulsen, J. C., Johansen, K. S., Krogh, K. B., Jorgensen, C. I., Tovborg, M., Anthonsen, A., Tryfona, T., Walter, C. P., Dupree, P., Xu, F., Davies, G. J., and Walton, P. H. (2011) Insights into the oxidative degradation of cellulose by a copper metalloenzyme that exploits biomass components. *Proc. Natl. Acad. Sci. U. S. A.* **108**, 15079-15084
7. Agger, J. W., Isaksen, T., Varnai, A., Vidal-Melgosa, S., Willats, W. G., Ludwig, R., Horn, S. J., Eijsink, V. G., and Westereng, B. (2014) Discovery of LPMO activity on hemicelluloses shows the importance of oxidative processes in plant cell wall degradation. *Proc. Natl. Acad. Sci. U. S. A.* **111**, 6287-6292
8. Isaksen, T., Westereng, B., Aachmann, F. L., Agger, J. W., Kracher, D., Kittl, R., Ludwig, R., Haltrich, D., Eijsink, V. G., and Horn, S. J. (2014) A C4-oxidizing lytic polysaccharide monooxygenase cleaving both cellulose and cello-oligosaccharides. *J. Biol. Chem.* **289**, 2632-2642
9. Vaaje-Kolstad, G., Westereng, B., Horn, S. J., Liu, Z., Zhai, H., Sorlie, M., and Eijsink, V. G. (2010) An oxidative enzyme boosting the enzymatic conversion of recalcitrant polysaccharides. *Science* **330**, 219-222
10. Forsberg, Z., Vaaje-Kolstad, G., Westereng, B., Bunaes, A. C., Stenstrom, Y., MacKenzie, A., Sorlie, M., Horn, S. J., and Eijsink, V. G. (2011) Cleavage of cellulose by a CBM33 protein. *Protein Sci.* **20**, 1479-1483
11. Hemsworth, G. R., Henrissat, B., Davies, G. J., and Walton, P. H. (2014) Discovery and characterization of a new family of lytic polysaccharide monooxygenases. *Nat. Chem. Biol.* **10**, 122-126
12. Lo Leggio, L., Simmons, T. J., Poulsen, J. C., Frandsen, K. E., Hemsworth, G. R., Stringer, M. A., von Freiesleben, P., Tovborg, M., Johansen, K. S., De Maria, L., Harris, P. V., Soong, C. L., Dupree, P., Tryfona, T., Lenfant, N., Henrissat, B., Davies, G. J., and Walton, P. H. (2015) Structure and boosting activity of a starch-degrading lytic polysaccharide monooxygenase. *Nat. Commun.* **6**, 5961
13. Tan, T. C., Kracher, D., Gandini, R., Sygmund, C., Kittl, R., Haltrich, D., Hallberg, B. M., Ludwig, R., and Divne, C. (2015) Structural basis for cellobiose dehydrogenase action during oxidative cellulose degradation. *Nat. Commun.* **6**, 7542
14. Westereng, B., Cannella, D., Wittrup Agger, J., Jorgensen, H., Larsen Andersen, M., Eijsink, V. G., and Felby, C. (2015) Enzymatic cellulose oxidation is linked to lignin by long-range electron transfer. *Sci. Rep.* **5**, 18561
15. Beeson, W. T., Phillips, C. M., Cate, J. H., and Marletta, M. A. (2012) Oxidative cleavage of cellulose by fungal copper-dependent polysaccharide monooxygenases. *J. Am. Chem. Soc.* **134**, 890-892

16. Kim, S., Stahlberg, J., Sandgren, M., Paton, R. S., and Beckham, G. T. (2014) Quantum mechanical calculations suggest that lytic polysaccharide monooxygenases use a copper-oxyl, oxygen-rebound mechanism. *Proc. Natl. Acad. Sci. U. S. A.* **111**, 149-154
17. Phillips, C. M., Beeson, W. T., Cate, J. H., and Marletta, M. A. (2011) Cellobiose dehydrogenase and a copper-dependent polysaccharide monooxygenase potentiate cellulose degradation by Neurospora crassa. *ACS Chem. Biol.* **6**, 1399-1406
18. Li, X., Beeson, W. T. t., Phillips, C. M., Marletta, M. A., and Cate, J. H. (2012) Structural basis for substrate targeting and catalysis by fungal polysaccharide monooxygenases. *Structure* **20**, 1051-1061
19. Vu, V. V., Beeson, W. T., Phillips, C. M., Cate, J. H., and Marletta, M. A. (2014) Determinants of regioselective hydroxylation in the fungal polysaccharide monooxygenases. *J. Am. Chem. Soc.* **136**, 562-565
20. Crawford, D. L. (1978) Lignocellulose decomposition by selected streptomyces strains. *Appl. Environ. Microbiol.* **35**, 1041-1045
21. Goodfellow, M., and Williams, S. T. (1983) Ecology of actinomycetes. *Annu. Rev. Microbiol.* **37**, 189-216
22. McCarthy, A. J., and Williams, S. T. (1992) Actinomycetes as agents of biodegradation in the environment. *Gene* **115**, 189-192
23. Takasuka, T. E., Book, A. J., Lewin, G. R., Currie, C. R., and Fox, B. G. (2013) Aerobic deconstruction of cellulosic biomass by an insect-associated Streptomyces. *Sci. Rep.* **3**, 1030
24. Nielsen, J. (1996) Modelling the morphology of filamentous microorganisms. *Trends Biotechnol.* **14**, 438-443
25. van Dissel, D., Claessen, D., and van Wezel, G. P. (2014) Morphogenesis of Streptomyces in submerged cultures. *Adv. Appl. Microbiol.* **89**, 1-45
26. Vrancken, K., and Anne, J. (2009) Secretory production of recombinant proteins by Streptomyces. *Future Microbiol.* **4**, 181-188
27. Anne, J., Maldonado, B., Van Impe, J., Van Mellaert, L., and Bernaerts, K. (2012) Recombinant protein production and streptomycetes. *J. Biotechnol.* **158**, 159-167
28. Xu, H., Chater, K. F., Deng, Z., and Tao, M. (2008) A cellulose synthase-like protein involved in hyphal tip growth and morphological differentiation in streptomyces. *J. Bacteriol.* **190**, 4971-4978
29. van Veluw, G. J., Petrus, M. L., Gubbens, J., de Graaf, R., de Jong, I. P., van Wezel, G. P., Wosten, H. A., and Claessen, D. (2012) Analysis of two distinct mycelial populations in liquid-grown Streptomyces cultures using a flow cytometry-based proteomics approach. *Appl. Microbiol. Biotechnol.* **96**, 1301-1312
30. Chaplin, A. K., Petrus, M. L., Mangiameli, G., Hough, M. A., Svistunenko, D. A., Nicholls, P., Claessen, D., Vijgenboom, E., and Worrall, J. A. (2015) GlxA is a new structural member of the radical copper oxidase family and is required for glycan deposition at hyphal tips and morphogenesis of Streptomyces lividans. *Biochem. J.* **469**, 433-444
31. van Dissel, D., Claessen, D., Roth, M., and van Wezel, G. P. (2015) A novel locus for mycelial aggregation forms a gateway to improved Streptomyces cell factories. *Microb. Cell Fact.* **14**, 44
32. Cantarel, B. L., Coutinho, P. M., Rancurel, C., Bernard, T., Lombard, V., and Henrissat, B. (2009) The Carbohydrate-Active EnZymes database (CAZy): an expert resource for Glycogenomics. *Nucleic Acids Res.* **37**, D233-238
33. Liman, R., Facey, P. D., van Keulen, G., Dyson, P. J., and Del Sol, R. (2013) A laterally acquired galactose oxidase-like gene is required for aerial development during osmotic stress in Streptomyces coelicolor. *PLoS One* **8**, e54112
34. Blundell, K. L., Wilson, M. T., Svistunenko, D. A., Vijgenboom, E., and Worrall, J. A. (2013) Morphological development and cytochrome c oxidase activity in Streptomyces lividans are dependent on the action of a copper bound Sco protein. *Open Biol.* **3**, 120163

35. Blundell, K. L., Hough, M. A., Vijgenboom, E., and Worrall, J. A. (2014) Structural and mechanistic insights into an extracytoplasmic copper trafficking pathway in Streptomyces lividans. *Biochem. J.* **459**, 525-538
36. Petrus, M. L., Vijgenboom, E., Chaplin, A. K., Worrall, J. A., van Wezel, G. P., and Claessen, D. (2016) The DyP-type peroxidase DtpA is a Tat-substrate required for GlxA maturation and morphogenesis in Streptomyces. *Open Biol.* **6**, 150149
37. Cruz-Morales, P., Vijgenboom, E., Iruegas-Bocardo, F., Girard, G., Yanez-Guerra, L. A., Ramos-Aboites, H. E., Pernodet, J. L., Anne, J., van Wezel, G. P., and Barona-Gomez, F. (2013) The Genome Sequence of Streptomyces lividans 66 Reveals a Novel tRNA-Dependent Peptide Biosynthetic System within a Metal-Related Genomic Island. *Genome Biol. Evol.* **5**, 1165-1175
38. Gasteiger, E., Gattiker, A., Hoogland, C., Ivanyi, I., Appel, R. D., and Bairoch, A. (2003) ExPASy: The proteomics server for in-depth protein knowledge and analysis. *Nucleic Acids Res* **31**, 3784-3788
39. Svistunenko, D. A., and Cooper, C. E. (2004) A new method of identifying the site of tyrosyl radicals in proteins. *Biophys. J.* **87**, 582-595
40. Kabsch, W. (2010) Xds. *Acta Crystallographica Section D-Biological Crystallography* **66**, 125-132
41. Winter, G. (2010) xia2: an expert system for macromolecular crystallography data reduction. *J. Appl. Crystallogr.* **43**, 186-190
42. Evans, P. R., and Murshudov, G. N. (2013) How good are my data and what is the resolution? *Acta crystallographica. Section D, Biological crystallography* **69**, 1204-1214
43. Langer, G., Cohen, S. X., Lamzin, V. S., and Perrakis, A. (2008) Automated macromolecular model building for X-ray crystallography using ARP/wARP version 7. *Nat Protoc* **3**, 1171-1179
44. Long, F., Vagin, A. A., Young, P., and Murshudov, G. N. (2008) BALBES: a molecular-replacement pipeline. *Acta Crystallogr. D* **64**, 125-132
45. Murshudov, G. N., Vagin, A. A., and Dodson, E. J. (1997) Refinement of macromolecular structures by the maximum-likelihood method. *Acta Crystallogr. D* **53**, 240-255
46. Emsley, P., and Cowtan, K. (2004) Coot: model-building tools for molecular graphics. *Acta Crystallogr. D* **60**, 2126-2132
47. Davis, I. W., Leaver-Fay, A., Chen, V. B., Block, J. N., Kapral, G. J., Wang, X., Murray, L. W., Arendall, W. B., 3rd, Snoeyink, J., Richardson, J. S., and Richardson, D. C. (2007) MolProbity: all-atom contacts and structure validation for proteins and nucleic acids. *Nucleic Acids Res.* **35**, W375-383
48. Vaaje-Kolstad, G., Houston, D. R., Riemen, A. H., Eijsink, V. G., and van Aalten, D. M. (2005) Crystal structure and binding properties of the Serratia marcescens chitin-binding protein CBP21. *J. Biol. Chem.* **280**, 11313-11319
49. Vaaje-Kolstad, G., Bohle, L. A., Gaseidnes, S., Dalhus, B., Bjoras, M., Mathiesen, G., and Eijsink, V. G. (2012) Characterization of the chitinolytic machinery of Enterococcus faecalis V583 and high-resolution structure of its oxidative CBM33 enzyme. *J. Mol. Biol.* **416**, 239-254
50. Wong, E., Vaaje-Kolstad, G., Ghosh, A., Hurtado-Guerrero, R., Konarev, P. V., Ibrahim, A. F., Svergun, D. I., Eijsink, V. G., Chatterjee, N. S., and van Aalten, D. M. (2012) The Vibrio cholerae colonization factor GbpA possesses a modular structure that governs binding to different host surfaces. *PLoS Pathog.* **8**, e1002373
51. Hemsworth, G. R., Taylor, E. J., Kim, R. Q., Gregory, R. C., Lewis, S. J., Turkenburg, J. P., Parkin, A., Davies, G. J., and Walton, P. H. (2013) The copper active site of CBM33 polysaccharide oxygenases. *J. Am. Chem. Soc.* **135**, 6069-6077
52. Forsberg, Z., Mackenzie, A. K., Sorlie, M., Rohr, A. K., Helland, R., Arvai, A. S., Vaaje-Kolstad, G., and Eijsink, V. G. (2014) Structural and functional characterization of a conserved pair of bacterial cellulose-oxidizing lytic polysaccharide monooxygenases. *Proc. Natl. Acad. Sci. U. S. A.* **111**, 8446-8451

53. Forsberg, Z., Rohr, A. K., Mekasha, S., Andersson, K. K., Eijsink, V. G., Vaaje-Kolstad, G., and Sorlie, M. (2014) Comparative study of two chitin-active and two cellulose-active AA10-type lytic polysaccharide monooxygenases. *Biochemistry* **53**, 1647-1656
54. Nakagawa, Y. S., Kudo, M., Loose, J. S., Ishikawa, T., Totani, K., Eijsink, V. G., and Vaaje-Kolstad, G. (2015) A small lytic polysaccharide monooxygenase from Streptomyces griseus targeting alpha- and beta-chitin. *FEBS J.* **282**, 1065-1079
55. Hemsworth, G. R., Davies, G. J., and Walton, P. H. (2013) Recent insights into copper-containing lytic polysaccharide mono-oxygenases. *Curr. Opin. Struct. Biol.* **23**, 660-668
56. Römling, U. (2002) Molecular biology of cellulose production in bacteria. *Res. Microbiol.* **153**, 205-212
57. Ross, P., Mayer, R., and Benziman, M. (1991) Cellulose biosynthesis and function in bacteria. *Microbiol. Rev.* **55**, 35-58
58. Peisach, J., and Blumberg, W. E. (1974) Structural implications derived from the analysis of electron paramagnetic resonance spectra of natural and artificial copper proteins. *Arch. Biochem. Biophys.* **165**, 691-708
59. Frandsen, K. E., Simmons, T. J., Dupree, P., Poulsen, J. C., Hemsworth, G. R., Ciano, L., Johnston, E. M., Tovborg, M., Johansen, K. S., von Freiesleben, P., Marmuse, L., Fort, S., Cottaz, S., Driguez, H., Henrissat, B., Lenfant, N., Tuna, F., Baldansuren, A., Davies, G. J., Lo Leggio, L., and Walton, P. H. (2016) The molecular basis of polysaccharide cleavage by lytic polysaccharide. *Nat. Chem. Biol.* **12**, 298-303
60. Banci, L., Bertini, I., Cantini, F., Felli, I. C., Gonnelli, L., Hadjiliadis, N., Pierattelli, R., Rosato, A., and Voulgaris, P. (2006) The Atx1-Ccc2 complex is a metal-mediated protein-protein interaction. *Nat. Chem. Biol.* **2**, 367-368
61. Dwarakanath, S., Chaplin, A. K., Hough, M. A., Rigali, S., Vijgenboom, E., and Worrall, J. A. (2012) Response to Copper Stress in Streptomyces lividans Extends beyond Genes under Direct Control of a Copper-sensitive Operon Repressor Protein (CsoR). *J. Biol. Chem.* **287**, 17833-17847
62. Mortazavi, A., Williams, B. A., McCue, K., Schaeffer, L., and Wold, B. (2008) Mapping and quantifying mammalian transcriptomes by RNA-Seq. *Nat. Methods* **5**, 621-628

FIGURE LEGENDS

Figure 1: Cu(II) binding to *Sli*LPMO10E at pH 5 and 20 ^{o}C. Changes in the Trp emission spectrum (inset) upon titration of 1 mM Cu(II)SO_4 to *Sli*LPMO10E (2 μM) and plotted as a function of [Cu(II)]/[*Sli*LPMO10E]. The arrow indicates the direction of the emission change and the stoichiometry of the reaction is indicated by the intersection of the two solid lines.

Figure 2: EPR spectra of *Sli*LPMO10E at pH 7 and 10 K. A) As purified magnified x 4, and B) loaded with 0.9 equivalents of Cu(II). The experimental spectrum in (B) (solid line) has been approximated by a linear combination (dotted line) of the simulated EPR signals Sim1 and Sim2. C) Simulated EPR spectra of the Cu(II) ion coordinated by three N ligands (Sim1) and by two N ligands (Sim2). The coloured dots on the two simulated spectra indicate the positions of the principal g-values used in the simulations, purple – g_x, green – g_y, red – g_z. Each simulated spectrum is labelled with the equidistant quartet tick marks, centered at g_z and showing the positions of lines originated from the hyperfine interaction of the of Cu(II) electron spin (S = 1/2) with the Cu nuclear spin (I = 3/2). The simulation parameters are given in Table 3.

Figure 3: Substrate binding and activity of *Sli*LPMO10E. Inset SDS-PAGE to monitor the binding of *Sli*LPMO10E to cellulose (filter paper) or squid-pen β-chitin. Fractions shown are untreated *Sli*LPMO10E, the protein content in the supernatant (unbound) or bound to the substrate (bound). MALDI-TOF analysis of *Sli*LPMO10E products from squid-pen β-chitin. DPn_{al} = aldonic acid, DPn_{-2} =

lactone or C4 ketoaldose, (measured MW). $DP4_{-2}$ $+Na^+$ (851.3), $DP4_{al}$ $+Na^+$ (869.3), $DP4_{al}^-$ $+2Na^+$ (891.3), $DP6_{-2}$ $+Na^+$ (1257.5), $DP6_{al}$ $+Na^+$ (1275.5), $DP6_{al}^-$ $+2Na^+$ (1297.5), $DP8_{-2}$ $+Na^+$ (1663.6), $DP8_{al}$ $+Na^+$ (1681.7), $DP8_{al}^-$ $+2Na^+$ (1703.6).

Figure 4: X-ray crystal structure of *Sli*LPMO10E. A) Cartoon representation with the core β-sheet fold shown in purple and the Loop 2 region displayed in violet. Disulfide bonds are shown in yellow and the Cu represented as a sphere. B) A stick representation of the active site. Coordinating His residues are coloured in silver and residues surrounding the first Cu coordination sphere shown in orange. Bonds to the Cu ion are indicated in dashed lines. C) Electrostatic surface representation of the proposed substrate-binding surface with W56 labelled and the location of the Cu indicated by a dashed circle.

Figure 5: A second metal binding site creates a metal mediated *Sli*LPMO10E dimer. A) Surface representation of the symmetry generated metal mediated dimer of *Sli*LPMO10E together with a $2F_o - F_c$ electron density map contoured at 1 σ of the Cu coordination site at the dimer interface. Cu ions are shown in spheres. B) Anomalous electron density maps contoured at 5 σ at X-ray wavelengths of 1.2 Å (above the Cu and Zn K-edges) and 1.33 Å (below the Zn but above the Cu K-edges) for the active and MMD sites.

Figure 6: Fluorescence stopped-flow kinetics of Cu(II) binding to *Sli*LPMO10E at pH 5 and 25 ^oC. A) Biphasic time courses and fits to a double exponential function on reacting 2.5 μM (after mixing) *Sli*LPMO10E with various [Cu(II)] as indicated. Inset first order rate constants for the fast (k_{obs1}; squares) and the slow (k_{obs2}; triangles) phase of Cu(II) binding as a function of [Cu(II)]. B) Stoichiometry of Cu(II) binding monitored by fluorescence amplitude changes to *Sli*LPMO10E (5 μM after mixing) pre-loaded with *sub* to *super* stoichiometric amounts of Cu(II), following rapid mixing with excess Cu(II). The fast phase (k_{obs1}; squares) titrates with a ~ 0.5 stoichiometry with the slow phase (k_{obs2}; triangles) being observed following completion of the fast phase and with a ~ 0.5 stoichiometry.

Figure 7: Thermodynamics of Cu(II) binding to *Sli*LPMO10E at pH 5 and 25 ^oC. An ITC thermogram and fit to a sequential binding model (solid line) upon titrating *Sli*LPMO10E with Cu(II). Thermodynamic parameters obtained are reported in Table 5. Inset reports the heat of dilutions from a buffer to buffer and a Cu(II) to buffer titration.

Figure 8: Kinetics and thermodynamics of Cu(II) binding to *Sli*LPMO10E-Ext at pH 5 and 25 ^oC. A) First order rate constants for the fast (k_{obs1}) phase of Cu(II) binding to *Sli*LPMO10E-Ext as a function of [Cu(II)]. B) Titration of Cu(II) to *Sli*LPMO10E-Ext plotted as a function of fractional saturation defined as $Y = 1 - \Delta F/\Delta FT$ where ΔF is the fluorescence change and ΔFT is the fluorescent change from zero to fully saturated *Sli*LPMO10E with Cu(II). C) ITC binding profile and fit to a single-site binding model (solid line) upon titrating *Sli*LPMO10E-Ext with Cu(II). Thermodynamic parameters obtained from the fit are reported in Table 5.

Figure 9: Mechanism of Cu(II) binding to *Sli*LPMO10E and the N-terminal extension variant *Sli*LPMO10E-Ext. Dissociation constants (K_d) and rates (k) for Cu(II) binding are reported, with ^aK_d from ITC measurements, ^bK_d from kinetic measurements and ^cK_d from both experimental approaches. N is the stoichiometry of Cu(II) binding. The g_z and A_z values determined by EPR for the two Cu(II) species in WT *Sli*LPMO10E are reported. The minimum number of ligands for Cu(II) is four. X represents either a H_2O or Cl ligand depending on the experimental conditions (*i.e.* high or low NaCl) with Cl more likely under the high NaCl conditions based on the g_z value obtained by EPR.

Table 1: Transcription analysis of the seven *lpmo* genes in *S. lividans*. RNA-seq data obtained and reported earlier in liquid minimal media and glucose/mannitol as a carbon source (61) were analyzed with the *S. lividans* 1326 genome sequence as input (37).

Gene	Protein	*S. lividans* 1326[a] (RPKM)[b]	*S. lividans* 1326 + Cu[a] (RPKM)[b]
SLI0440	*Sli*LPMO10A	0	0
SLI0614	*Sli*LPMO10B	10	9
SLI1466	*Sli*LPMO10C	0	6
SLI2039	*Sli*LPMO10D	0	2
SLI3182	*Sli*LPMO10E	22	27
SLI6742	*Sli*LPMO10F	0	0
SLI7441	*Sli*LPMO10G	0	3

[a]The transcriptomes of WT *S. lividans* 1326 was obtained without addition of Cu to the growth medium. The Cu induced transcriptome was obtained after a 2 hour exposure to 400 μM Cu(II). [b]The selected expression measure is the RPKM and defined as the reads/kb of exon/million mapped reads *i.e.* dividing the total number of exon reads (in this case one exon per reference sequence) by the number of mapped reads (in millions) times the exon length (in kb) (62).

Table 2: Crystallographic data processing and refinement statistics. Values in parentheses refer to the outermost resolution shells (1.40-1.38, 2.07-2.02, 2.07-2.01 Å, respectively). The unit cell was a = 69.6, b = 32.4, c = 61.3 Å, β = 97.8° in space group C2.

Wavelength (Å)	1.0	1.33	1.20
Resolution (Å)	1.38	2.02	2.01
Unique reflections	27360	8755	8844
Completeness (%)	97.3 (92.2)	97.6 (90.6)	96.7 (87.2)
R_{merge}	0.055 (0.680)	0.060 (0.087)	0.049 (0.084)
Mn(I/sd)	14.8 (1.8)	20.3 (13.7)	24.1 (15.9)
Redundancy	4.9 (3.5)	5.5 (4.7)	5.5 (4.7)
Wilson B-factor ($Å^2$)	9.3	8.3	9.8
R_{cryst}	0.135		
R_{free}	0.160		
ESU based on ML (Å)	0.038		
RMS dev. Bond lengths (Å)	0.017		
RMS dev. Bond angles (°)	1.72		
Ramachandran favoured (%)	98.8		
PDB accession code	5ftz		

Table 3: The EPR simulation parameters of *Sli*LPMO10E used to simulate spectra Sim1 and Sim 2 in Figure 3.

		g	A^{Cu} (G)	A^{N} (G)	ΔH (G)
Sim1[a]	x	2.033	13.5	14	12
	y	2.067	13.5	14	13
	z	2.260	135	14	26
Sim2[b]	x	2.055	19	14	12
	y	2.071	19	14	13
	z	2.230	190	14	23

[a]Simulated for three coordinating N atoms. [b]Simulated for two coordinating N atoms

Table 4: Bond lengths and angles of active site and symmetry related metal mediated dimer site (MMD).

Bond	Length/Angle (Å, °)
Active site	
His^{30} Nδ1	1.94
His^{30} N	2.24
His^{120} Nε2	1.91
His^{30} Nδ1 -Cu- His^{120} N	95
His^{30} Nδ1 -Cu- His^{120} Nε2	160
His^{30} N -Cu- His^{120} Nε2	103
MMD site	
His^{187} Nε2	1.95
Asp^{188} Oδ2	2.40
His^{187} Nε2*	1.94
Asp^{188} Oδ2*	2.42

*Symmetry related molecule

Table 5: Kinetic and thermodynamic parameters determined from stopped-flow fluorescence, fluorescence titrations and ITC at 25 °C for Cu(II) binding to the various forms of *Sli*LPMO10E.

[a]Fluorescence					
Protein	k_1 ($M^{-1}s^{-1}$)	k_2 ($M^{-1}s^{-1}$)	k_2 (s^{-1})	k_3 (s^{-1})	K_d (M)
*Sli*LPMO10E	6.6 (0.3) x 10^5	2.2 (0.04) x 10^4	-	-	-
H187A	3.6 (0.3) x 10^5	9.2 (0.3) x 10^3	-	-	-
*Sli*LPMO10E-Ext	2.0 (0.2) x 10^6	-	60 (1.7)	0.2 (0.01)	[b]2.4 x 10^{-6} [c]0.5 x 10^{-6}
*Sli*LPMO10B	1.0 (0.1) x 10^6	5.0 (0.2) x 10^4	-	-	-

[d]ITC					
Protein	*N*	K_d (M)	ΔG_b (kcal mol^{-1})	ΔH_b (kcal mol^{-1})	$-T\Delta S$ (kcal mol^{-1})
[e]*Sli*LPMO10E	0.48 (0.02)	62.5 (0.2) x 10^{-9}	-9.8 (0.3)	-7.9 (0.4)	-1.9 (0.8)
	0.43 (0.05)	4.2 (0.6) x 10^{-6}	-7.3 (0.2)	2.3 (0.5)	-9.6 (0.3)
[e]H187A	0.40 (0.05)	55.8 (2.0) x 10^{-9}	-9.9 (0.8)	-7.9 (0.2)	-2.0 (0.1)
	0.42 (0.1)	4.1 (0.2) x 10^{-6}	-7.4 (0.9)	2.5 (0.4)	-9.9 (0.3)
[f]*Sli*LPMO10E-Ext	0.94 (0.1)	2.6 (0.1) x 10^{-6}	-7.6 (0.5)	20.0 (2.1)	-27.6 (1.1)

[a]Experimental errors are reported in parenthesis and are the standard errors from triplicate experiments [b]Determined from static fluorescence titration. [c]Determined from stopped-flow fluorescence. [d]Experimental errors are reported in parenthesis and are the standard errors from triplicate experiments for *Sli*LPMO10E and duplicates for H187A and *Sli*LPMO10E-EXT. [e]Parameters derived from a sequential binding model. [f]Parameters derived from a one set of sites binding model.

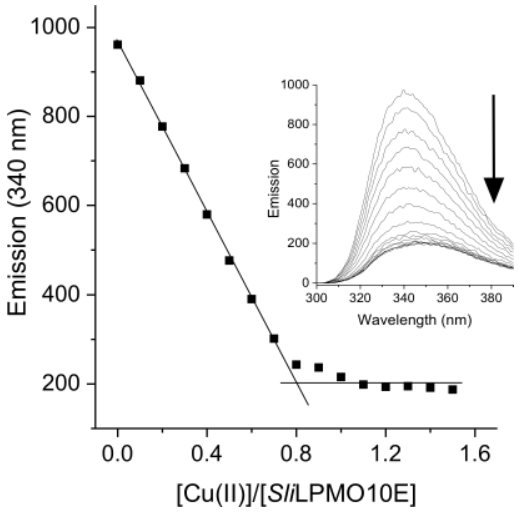
Emission (340 nm)
1000
800
600
400
200
0.0
0.4
0.8
1.2
1.6
[Cu(II)]/[SliLPMO10E]
Emission
Wavelength (nm)
300
320
340
360
380

Figure 1

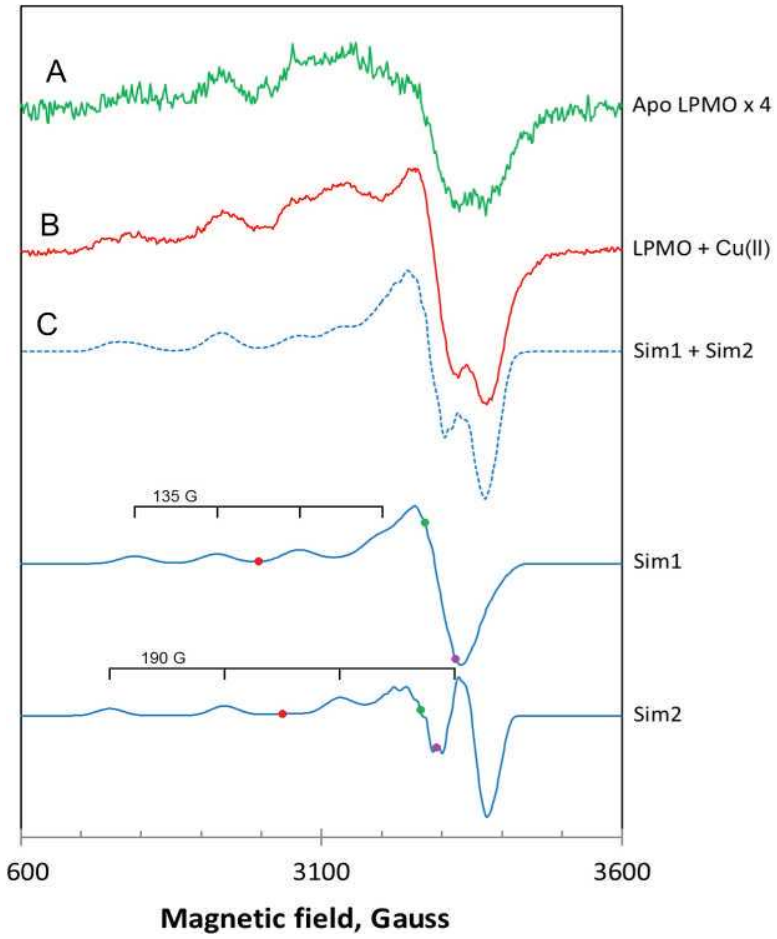
A
Apo LPMO x 4
B
LPMO + Cu(II)
C
Sim1 + Sim2
135 G
Sim1
190 G
Sim2
600
3100
3600
Magnetic field, Gauss

Figure 2

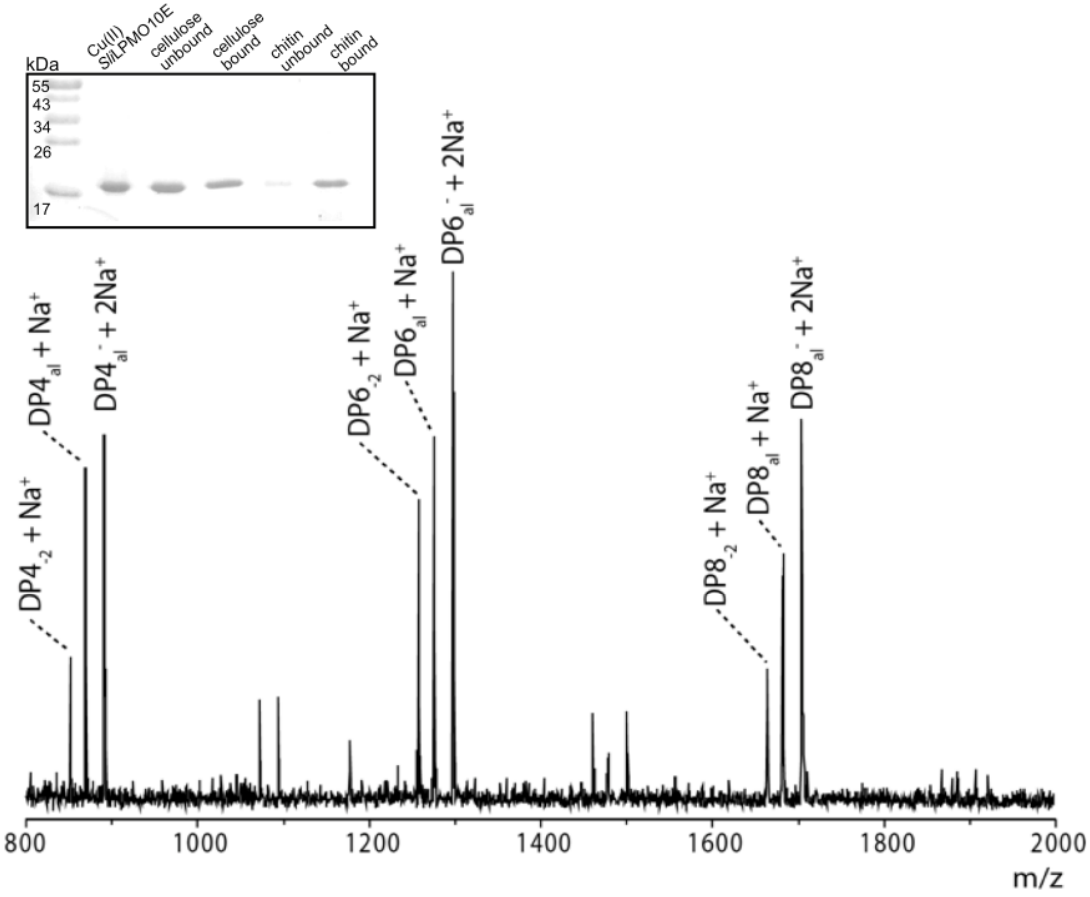
Cu(II) SlLPMO10E
cellulose unbound
cellulose bound
chitin unbound
chitin bound
kDa
55
43
34
26
17
DP4-2 + Na+
DP4al + Na+
DP4al- + 2Na+
DP6-2 + Na+
DP6al + Na+
DP6al- + 2Na+
DP8-2 + Na+
DP8al + Na+
DP8al- + 2Na+
800
1000
1200
1400
1600
1800
2000
m/z

Figure 3

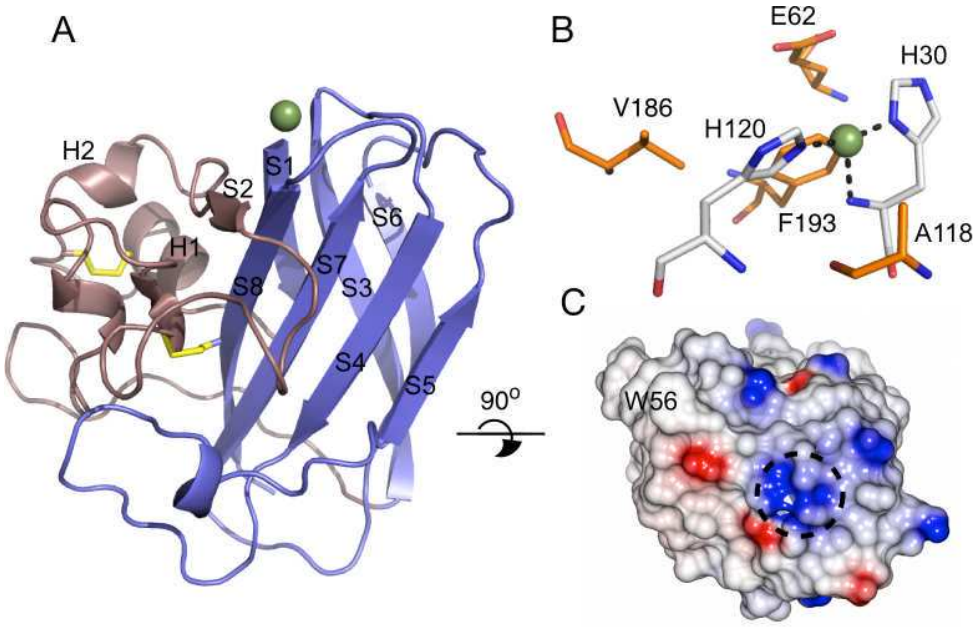
A
H2
S1
S2
S6
H1
S7
S8
S3
S4
S5
90°
B
E62
H30
V186
H120
F193
A118
C
W56

Figure 4

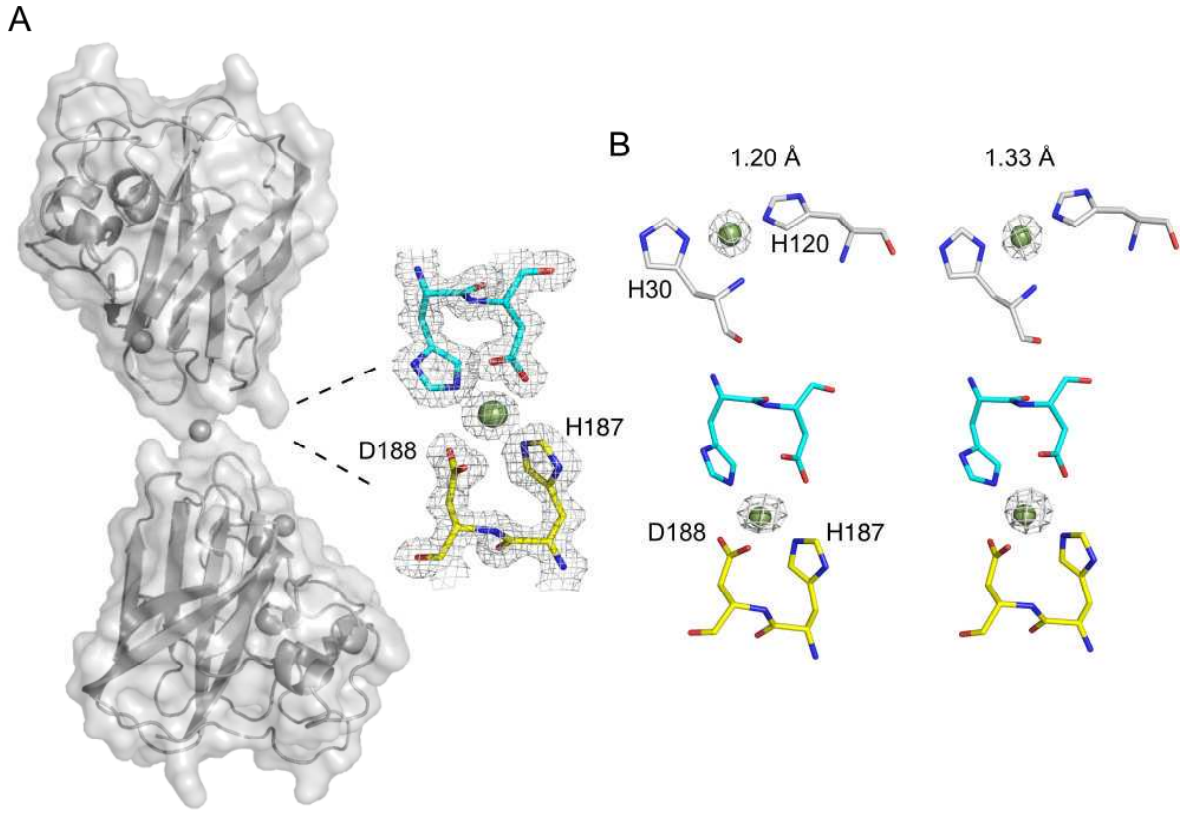

Figure 5

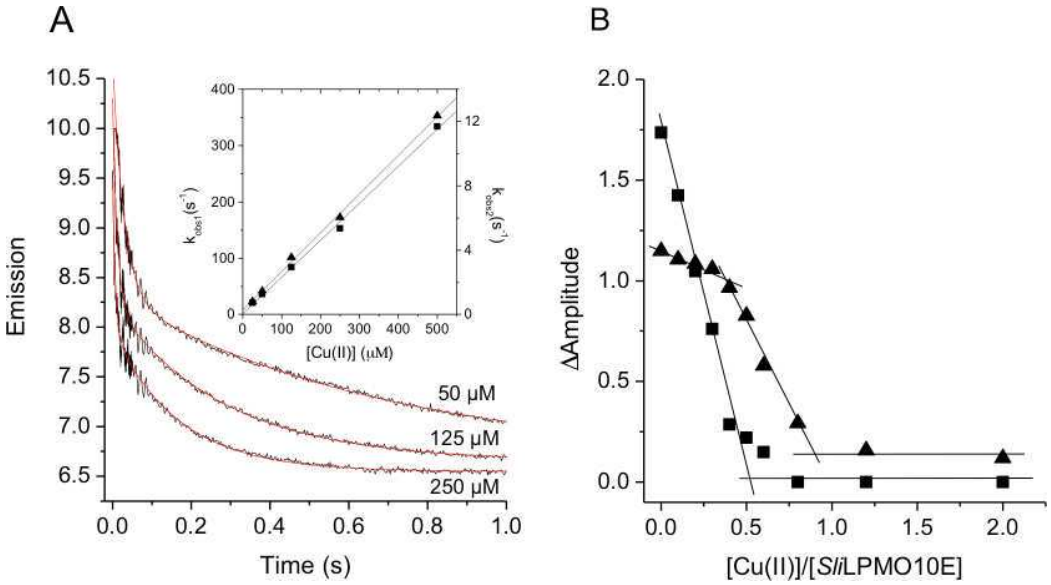
A
B
Emission
Time (s)
50 µM
125 µM
250 µM
[Cu(II)] (µM)
ΔAmplitude
[Cu(II)]/[SliLPMO10E]

Figure 6

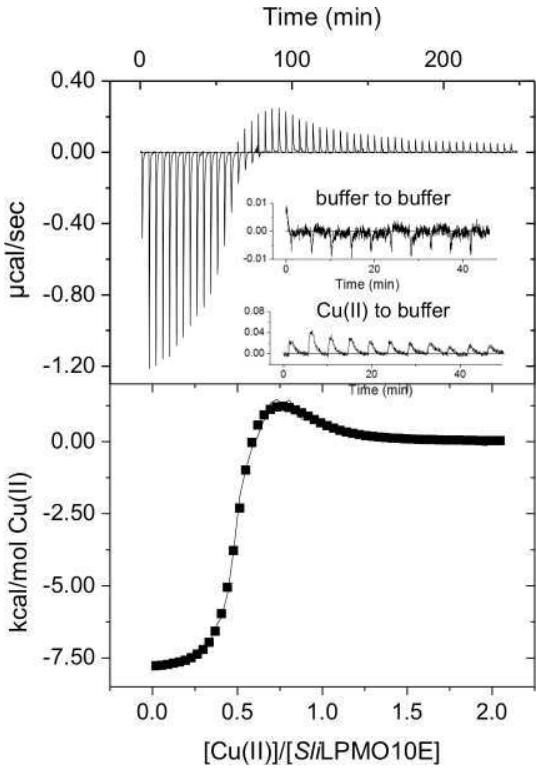
Time (min)
0
100
200
0.40
0.00
-0.40
-0.80
-1.20
µcal/sec
buffer to buffer
0.01
0.00
-0.01
0
20
40
Time (min)
Cu(II) to buffer
0.08
0.04
0.00
0
20
40
Time (min)
0.00
-2.50
-5.00
-7.50
kcal/mol Cu(II)
0.0
0.5
1.0
1.5
2.0
[Cu(II)]/[SliLPMO10E]

Figure 7

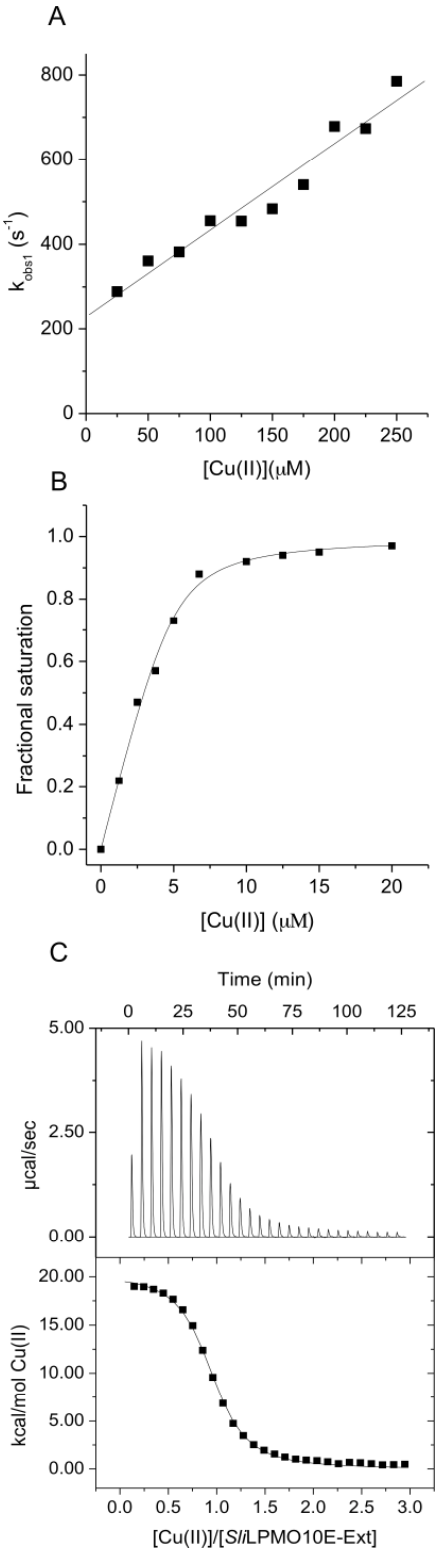
A
800
600
400
200
0
k_{obs1} (s^{-1})
0
50
100
150
200
250
[Cu(II)](μM)
B
1.0
0.8
0.6
0.4
0.2
0.0
Fractional saturation
0
5
10
15
20
[Cu(II)] (μM)
C
Time (min)
0
25
50
75
100
125
5.00
2.50
0.00
μcal/sec
20.00
15.00
10.00
5.00
0.00
kcal/mol Cu(II)
0.0
0.5
1.0
1.5
2.0
2.5
3.0
[Cu(II)]/[*Sli*LPMO10E-Ext]

Figure 8

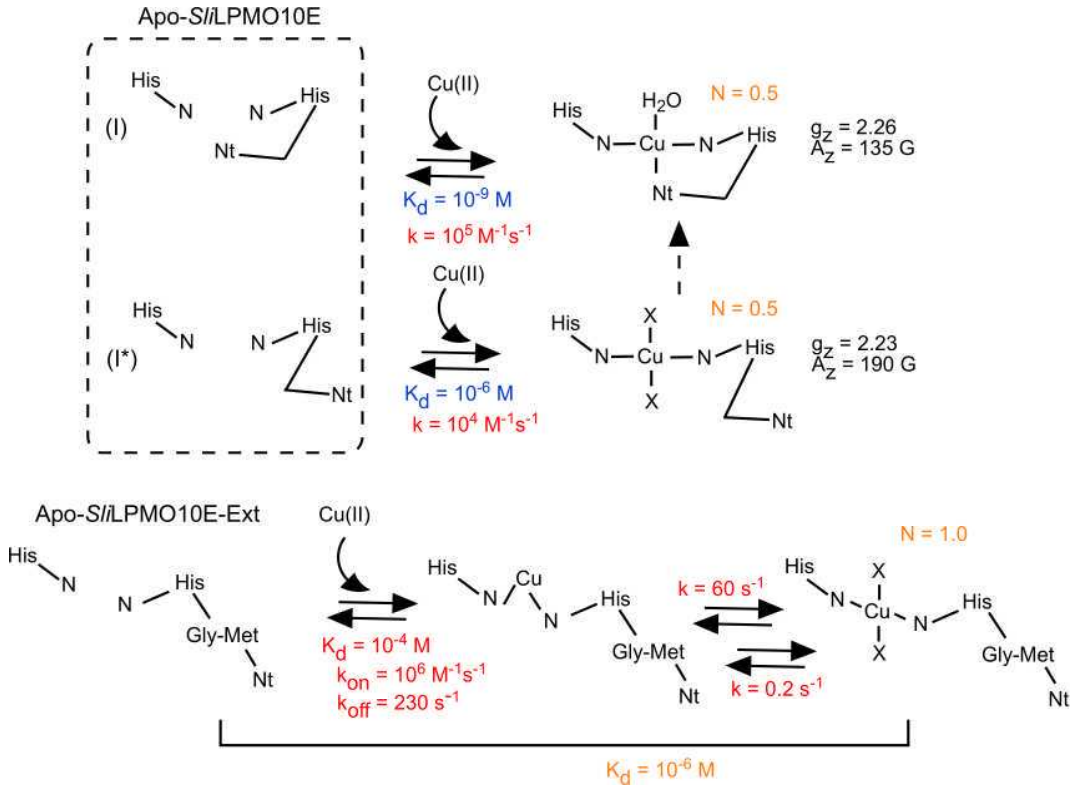
Apo-SliLPMO10E
(I)
(I*)
His
N
Nt
Cu(II)
K_d = 10^{-9} M
k = 10^5 $M^{-1}s^{-1}$
K_d = 10^{-6} M
k = 10^4 $M^{-1}s^{-1}$
H_2O
N = 0.5
g_z = 2.26
A_z = 135 G
g_z = 2.23
A_z = 190 G
Cu
X
Apo-SliLPMO10E-Ext
Gly-Met
K_d = 10^{-4} M
k_{on} = 10^6 $M^{-1}s^{-1}$
k_{off} = 230 s^{-1}
k = 60 s^{-1}
k = 0.2 s^{-1}
N = 1.0
K_d = 10^{-6} M

Figure 9